PCCP
Physical Chemistry Chemical Physics

Accepted Manuscript

This article can be cited before page numbers have been issued, to do this please use: O. Long, G. Sai Gautam and E. A. Carter, *Phys. Chem. Chem. Phys.*, 2021, DOI: 10.1039/D1CP03163E.

ROYAL SOCIETY OF CHEMISTRY

rsc.li/pccp

View Article Online
DOI: 10.1039/D1CP03163E

Assessing cathode property prediction via exchange-correlation functionals with and without long-range dispersion corrections

Olivia Y. Long,[1,2] Gopalakrishnan Sai Gautam,[3,4] and Emily A. Carter[3,5,*]

[1]Department of Physics, Princeton University, Princeton, New Jersey 08544, USA
[2]Department of Applied Physics, Stanford University, Stanford, California 94305, USA
[3]Department of Mechanical and Aerospace Engineering, Princeton University, Princeton, New Jersey 08544, USA
[4]Department of Materials Engineering, Indian Institute of Science, Bengaluru, Karnataka 560012, India
[5]Office of the Chancellor and Department of Chemical and Biomolecular Engineering, University of California, Los Angeles, Los Angeles, California 90095, USA
[*]E-mail: eac@ucla.edu

Abstract

We benchmark calculated interlayer spacings, average topotactic voltages, thermodynamic stabilities, and band gaps in layered lithium transition-metal oxides (TMOs) and their de-lithiated counterparts, which are used in lithium-ion batteries as positive electrode materials, against available experimental data. Specifically, we examine the accuracy of properties calculated within density functional theory (DFT) using eight different treatments of electron exchange-correlation: the strongly constrained and appropriately normed (SCAN) and Perdew-Burke-Ernzerhof (PBE) density functionals, Hubbard-*U*-corrected SCAN and PBE (i.e., SCAN+*U* and PBE+*U*), and SCAN(+*U*) and PBE(+*U*) with added long-range dispersion (D) interactions (i.e., DFT(+*U*)+D). van der Waals interactions are included respectively via the revised Vydrov-Van Voorhis (rVV10) for SCAN(+*U*) and the DFT-D3 for PBE(+*U*). We find that SCAN-based functionals predict larger voltages due to an underestimation of stability of the MO_2 systems, while also predicting smaller interlayer spacings compared to their PBE-based counterparts. Furthermore, adding dispersion corrections to PBE has a greater effect on voltage predictions and interlayer spacings than with SCAN, indicating that DFT-SCAN – despite being a ground-state theory – fortuitously captures some short and medium-range dispersion interactions better than PBE. While SCAN-based and PBE-based functionals yield qualitatively similar band gap predictions, there is no significant quantitative improvement of SCAN-based functionals over the corresponding PBE-based versions. Finally, we expect SCAN-based functionals to yield more accurate property predictions than the respective PBE-based functionals for most TMOs, given SCAN's stronger theoretical

View Article Online
DOI: 10.1039/D1CP03163E

underpinning and better predictions of systematic trends in interlayer spacings, intercalation voltages, and band gaps obtained in this work.

Introduction

Lithium-ion rechargeable batteries (LIBs) have revolutionized the electronics industry and modern communication, while reducing dependence on fossil fuels (via electrification of ground transport) and promoting more sustainable energy consumption (grid-scale storage to modulate intermittent renewable sources).[1–9] Due to the growing global demand, it is desirable to increase the energy density and decrease the cost of such LIBs.[2,3,9,10] State-of-the-art LIBs typically utilize a cathode framework that can reversibly intercalate Li ions against another intercalation anode (typically graphite), separated by a liquid electrolyte (usually organic solvents).[11] Thus, the energy density of a given LIB is largely determined by the properties of the cathode, specifically the product of the intercalation voltage (that the cathode exhibits against the anode) and the specific capacity (related to the number of Li intercalation sites available in the cathode framework). A robust computational scheme to determine these two factors could aid considerably in the screening and design of new cathode materials. The work in this paper is an attempt to form such a computational approach.

To date, one of the most promising battery cathode classes are layered 3*d* transition-metal oxides (TMOs),[4,12,13] given the high intercalation voltages that these layered oxides can exhibit in addition to the high number of available Li intercalation sites per formula unit. For computational modeling of battery electrodes based on density functional theory (DFT),[14,15] it is important to capture accurately the redox behavior of the 3*d* transition-metal ions contained in them. However, due to self-interaction errors (SIEs),[16,17] exchange-correlation (XC) functionals, such as the

View Article Online
DOI: 10.1039/D1CP03163E

strongly constrained and appropriately normed (SCAN)[18] and the Perdew-Burke-Ernzerhof (PBE)[19] generalized gradient approximation (GGA) functionals, suffer from inaccurate predictions of important properties, including electronic structures, thermodynamic stabilities, and ground-state crystal structures.[17,20–23] Such errors in modeling 3*d* TMOs can be corrected by applying an optimal Hubbard *U* parameter,[24,25] as demonstrated with PBE and SCAN in previous studies.[23,26,27] Even with such corrections, DFT functionals are not expected to describe accurately dispersion (i.e., van der Waals) forces, which are nonlocal and inherently involve excited states (induced dipole-induced dipole interactions).[28,29]

To model accurately systems with nonbonded interactions, such as layered lithium TMOs, it is important to account for van der Waals forces in the theoretical framework. Specifically, $LiMO_2$ with M = V, Cr, Mn, Fe, Co, Ni, and Cu are notable for their role as cathode (i.e., positive electrode) materials in LIB applications.[1] Note that the $LiMO_2$ oxides are layered in the sense that Li, M, and O atoms are arranged across distinct planes (or layers) along the *c*-axis (**Figure 1**). During charging and discharging, lithium ions are deintercalated and intercalated from the metal oxide layers, respectively.[30] Since the weak van der Waals forces between oxygen ions of adjacent MO_2 layers are nonlocal, particularly at low lithium contents, they are not well captured by commonly used functionals such as PBE. Efforts to treat such interactions have yielded dispersion-corrected functionals such as the widely-used DFT-D3 functional[31] (typically used with PBE), which has been shown to describe well both van der Waals forces and noncovalent interactions within molecules.[31,32] While SCAN has been reported to reproduce some medium-range dispersion interactions,[18,33] it may also need the addition of a separate van der Waals functional to accurately model layered systems.[34] Given the plethora of battery applications of layered lithium TMOs, it is desirable to predict accurately properties such as the interlayer spacing, intercalation voltages, and

View Article Online
DOI: 10.1039/D1CP03163E

electronic structure of such systems as we work to develop even better battery storage technologies.

In this work, we assess the interlayer distance (*c* lattice parameter), the average topotactic voltage, the thermodynamic stability, and the band gap of layered lithium TMOs and their de-lithiated (i.e., Li-removed) counterparts using eight different XC treatments and benchmark them against available experimental data. We consider compositions of the form $LiMO_2$ and MO_2, where M = V, Cr, Mn, Fe, Co, Ni, and Cu (i.e., all 3*d* metals excluding Sc, Ti, and Zn). Chief of our eight functionals is the SCAN meta-GGA, which satisfies the 17 known constraints of an XC functional.[18,33] Additionally, we employ the Hubbard *U* corrected[24] SCAN, i.e., the SCAN+*U*[23] functional, to correct spurious SIEs in TMOs. To examine the impact of long-range dispersion corrections, we calculate properties with and without the revised Vydrov-Van Voorhis (rVV10)[35,36] functional, which is the only van der Waals functional that has been parameterized for SCAN(+*U*).[34] Since PBE is currently one of the most used DFT XC functionals, we also assess the accuracy of the PBE(+*U*) functional with and without long-range dispersion corrections (using the DFT-D3 functional) in predicting the abovementioned properties. Thus, for each composition, we consider the following XC treatments: SCAN, PBE, SCAN+*U*, PBE+*U,* SCAN+rVV10, PBE+D3, SCAN+*U*+rVV10, and PBE+*U*+D3. Besides benchmarking the accuracy of these eight XC approximations against experimental data, we highlight notable systems such as $LiMnO_2$ and $LiCoO_2$ to illustrate the general trends observed, as well as anomalies to the observed trends (e.g., $LiFeO_2$).

Methods

View Article Online
DOI: 10.1039/D1CP03163E

We utilized the Vienna ab initio simulation package (VASP)[37,38] to perform DFT calculations within the all-electron, frozen-core, projector augmented-wave (PAW) formalism.[39,40] Since SCAN-derived PAW potentials are not yet available for several elements, we used VASP's PAW potentials derived at the PBE level, consistent with our previous work.[23,27] We used a kinetic energy cutoff of 520 eV for the planewave basis and a dense, Γ-point-centered, Monkhorst-Pack[41] *k*-point mesh (spacing $\leq$ 0.025 Å^{-1}) to sample the Brillouin zone. Additionally, we used Gaussian smearing[42] to integrate over the Fermi surface, with a smearing width of 0.05 eV. For PBE+*U*(+D3) and SCAN+*U*(+rVV10) calculations, the *U* was input according to the rotationally invariant framework of Dudarev *et al*.[43] In the case of PBE+*U*(+D3) calculations, we used the *U* values from the Materials Project,[44] while for SCAN+*U*(+rVV10) calculations we used the *U* values derived in our previous work.[23,27] The initial structures of all $LiMO_2$ compositions were obtained from the inorganic crystal structure database (ICSD).[45] We relaxed the lattice vectors, volume, and ionic positions of all the oxides, with the relaxation terminated once the total energies and atomic forces converged to < 0.01 meV and < |0.03| eV/Å, respectively. We calculated all band gaps at the Kohn-Sham (KS) DFT level because our previous work indicated a high degree of correlation between qualitatively consistent KS eigenvalue gaps and accurate redox enthalpies, lattice parameters, and polymorph selection in transition-metal and rare-earth oxides.[23,27] Band gaps reported here are based on total density of states (DOS) calculations, where we sampled electronic energies at intervals of 0.005 eV. Note that SCAN does improve band gap estimates in solids compared to PBE at the generalized Kohn-Sham (gKS) level of theory.[46]

Topotactic Li-intercalation reactions occur when the underlying host structure does not change significantly during the addition or removal of Li ions,[47] as shown in **Figure 1**. Such reactions in layered $LiMO_2$ cathodes are most relevant for battery applications, due to their high

View Article Online
DOI: 10.1039/D1CP03163E

capacity and rate capability compared to other structures.[48,49] We therefore calculated the average voltages of the $LiMO_2/MO_2$ systems considered using the topotactic structures (i.e., MO_2 structures derived from Li-deficient $LiMO_2$ structures) using the following approximate formula:

$$\langle V \rangle = -\frac{E_{\mathrm{LiMO_2}} - E_{\mathrm{MO_2}} - E_{\mathrm{Li}}}{nF} \quad (1)$$

where n is the number of electrons transferred by the Li ion, F is the Faraday constant, and E is the DFT total energy of a given species at zero K. E_{Li} is the total energy of Li metal in its ground-state body-centered-cubic structure. We approximated the Gibbs free energy with the corresponding E, ignoring entropic and pressure-volume effects, since these effects are known to not impact average intercalation voltages significantly.[47,50,51]

View Article Online
DOI: 10.1039/D1CP03163E

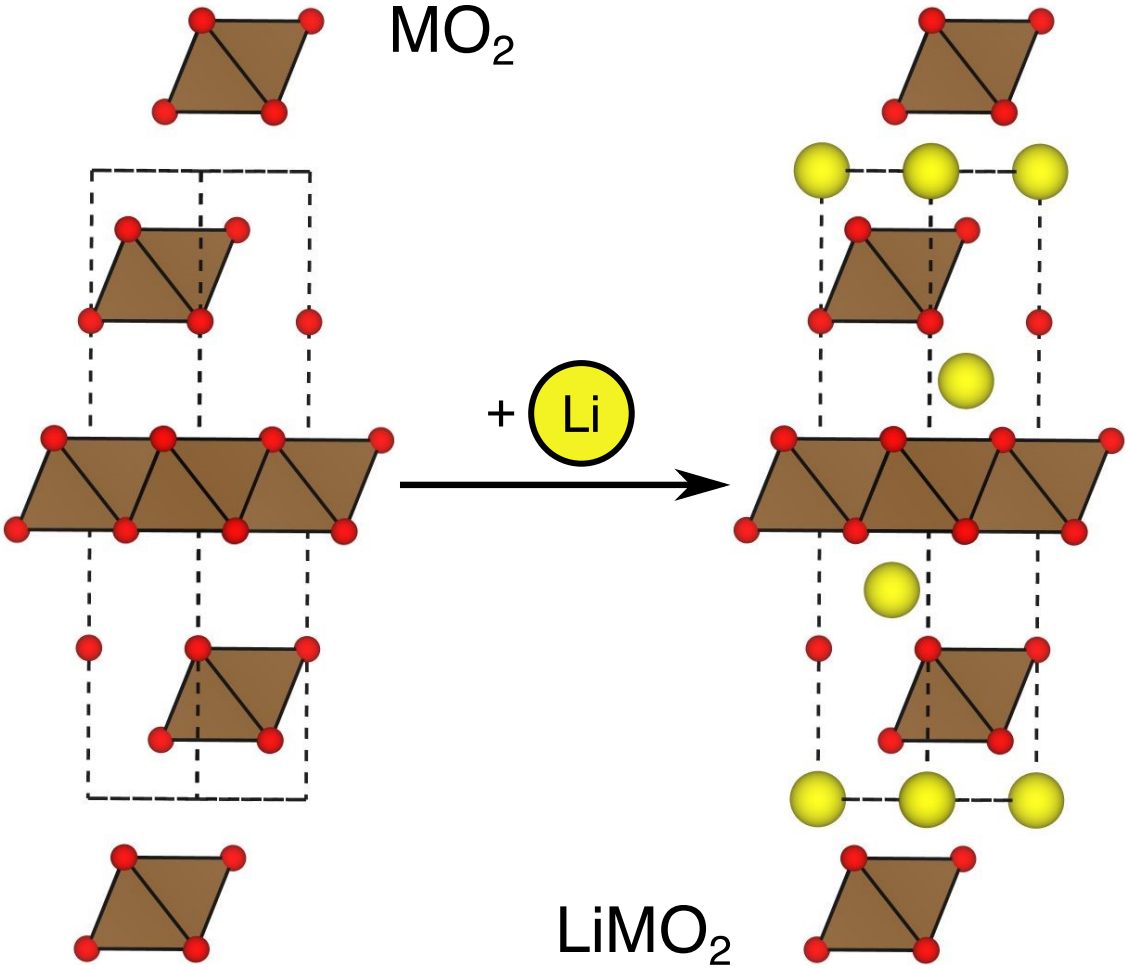

Figure 1: Schematic of a typical topotactic intercalation process, where Li intercalation in a layered MO_2 yields a $LiMO_2$ structure with minimal changes to the underlying MO_2 framework. Li and O atoms are indicated by the yellow and red spheres while transition metal cations occupy the center of each brown polyhedron.

The stabilities of the $LiMO_2$ and MO_2 systems were evaluated by comparing the compositions to competing stable phases with, ideally, the same oxidation state of the metal ion (e.g., M^{3+} in $LiMO_2$). This relative stability serves as a proxy for the energy above the convex hull, i.e., the 0 K phase diagram of the Li-M-O (or M-O) system. Computation of the convex hull requires considering all possible compounds that can form in each of the Li-M-O composition spaces, which is computationally demanding, especially considering the eight different XC models used in this work. For the $LiMO_2$ systems with stable M_2O_3 phases (M = V, Cr, Mn, Fe), a possible formation reaction can be written as $0.5(Li_2O + M_2O_3) \rightarrow LiMO_2$. Thus, we evaluate the stability

View Article Online
DOI: 10.1039/D1CP03163E

of $LiMO_2$ with respect to Li_2O and M_2O_3 compounds, as in **Eq. 2**, where all E terms correspond to the calculated total energies for each compound considered.

$$\text{Stability}\left(LiMO_2\right) = E_{LiMO_2} - 0.5\left(E_{Li_2O} + E_{M_2O_3}\right) \quad (2)$$

If the system does not have a stable M_2O_3 phase, the stable phase with the closest oxidation state was used. For example, in the cases of $LiCoO_2$, $LiNiO_2$, and $LiCuO_2$, the stable phases of Co_3O_4 (Co^{2+}/Co^{3+}), NiO (Ni^{2+}), and CuO (Cu^{2+}) were used, respectively, in conjunction with Li_2O and O_2 (gas), as indicated by the set of equations below.

$$\text{Stability}\left(LiCoO_2\right) = E_{LiCoO_2} - 0.5\left(E_{Li_2O}\right) - 0.33\left(E_{Co_3O_4}\right) - 0.083\left(E_{O_2(g)}\right) \quad (3)$$

$$\text{Stability}\left(LiNiO_2\right) = E_{LiNiO_2} - 0.5\left(E_{Li_2O}\right) - \left(E_{NiO}\right) - 0.25\left(E_{O_2(g)}\right) \quad (4)$$

$$\text{Stability}\left(LiCuO_2\right) = E_{LiCuO_2} - 0.5\left(E_{Li_2O}\right) - \left(E_{CuO}\right) - 0.25\left(E_{O_2(g)}\right) \quad (5)$$

Similarly, the stabilities of the topotactic structures of MO_2 were evaluated using the ground-state structure of the same composition, if stable. For example, layered VO_2, CrO_2, and MnO_2 are metastable and we computed their metastability with respect to the corresponding ground-state phases, namely rutile polymorphs of VO_2, CrO_2, and MnO_2, respectively, as shown in **Eq. 6**.

$$\text{Stability}\left(MO_2\right) = E_{MO_2}(layered) - E_{MO_2}(rutile) \quad (6)$$

FeO_2, CoO_2, NiO_2, and CuO_2 were compared to the stable phases with the closest oxidation states to M^{4+}, namely, Fe_2O_3 (Fe^{3+}), Co_3O_4 (Co^{2+}/Co^{3+}), NiO (Ni^{2+}), and CuO (Cu^{2+}), respectively, alongside O_2 (gas), as displayed in the following equations.

$$\text{Stability}\left(FeO_2\right) = E_{FeO_2}(layered) - 0.5\left(E_{Fe_2O_3}\right) - 0.25\left(E_{O_2(g)}\right) \quad (7)$$

$$\text{Stability}\left(CoO_2\right) = E_{CoO_2}(layered) - 0.33\left(E_{Co_3O_4}\right) - 0.33\left(E_{O_2(g)}\right) \quad (8)$$

$$\text{Stability}\left(NiO_2\right) = E_{NiO_2}(layered) - \left(E_{NiO}\right) - 0.5\left(E_{O_2(g)}\right) \quad (9)$$

$$\text{Stability}\left(CuO_2\right) = E_{CuO_2}(layered) - \left(E_{CuO}\right) - 0.5\left(E_{O_2(g)}\right) \quad (10)$$

View Article Online
DOI: 10.1039/D1CP03163E

Results

Interlayer Spacing

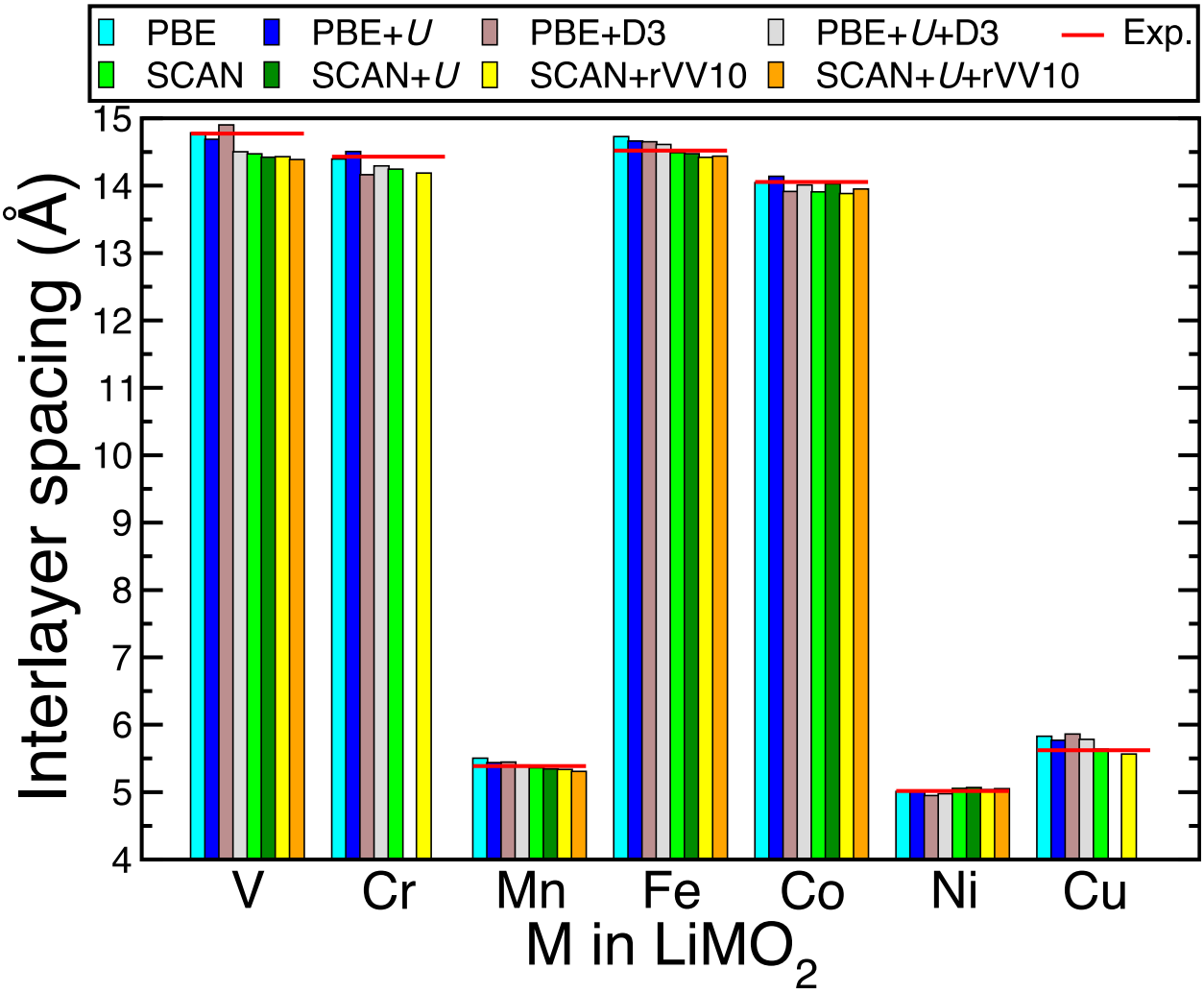

Figure 2: Interlayer spacing (*c* lattice parameter) calculated by PBE (light blue bars), PBE+*U* (dark blue), PBE+D3 (brown), PBE+*U*+D3 (grey), SCAN (light green), SCAN+*U* (dark green), SCAN+rVV10 (yellow), and SCAN+*U*+rVV10 (orange) for the seven $LiMO_2$ systems considered. Horizontal red lines indicate experimental values. Cr and Cu do not have bars for SCAN+*U* and SCAN+*U*+rVV10 since a *U* correction is not needed with SCAN for these elements.[27] $LiMnO_2$, $LiNiO_2$, and $LiCuO_2$ exhibit a single layer each of M and Li, while the other oxides exhibit three layers each of M and Li.

Since the structural stability of layered $LiMO_2$ mainly depends on the interlayer distance (*c* parameter), we compare the calculated *c* parameters of the eight XC models considered versus experimental data[52] in **Figure 2** for all $LiMO_2$ structures. $LiVO_2$, $LiCrO_2$, $LiFeO_2$, and $LiCoO_2$

View Article Online
DOI: 10.1039/D1CP03163E

exhibit the hexagonal, layered structure in the $R\bar{3}mH$ spacegroup (commonly referred to as O3-type layered structures), while $LiMnO_2$, $LiNiO_2$ and $LiCuO_2$ adopt a layered structure with a monoclinic distortion, in the $C12/m1$ or $C2/m$ spacegroups. The origin of the monoclinic distortion in $LiMnO_2$ and $LiNiO_2$ is the well-known Jahn-Teller distortion[53,54] of Mn^{3+} and Ni^{3+} cations, which results in a O1-type layered structure. In the case of $LiCuO_2$, the monoclinic distortion originates from the unique square-planar coordination environment exhibited by Cu^{3+} ions and also results in a O1-type structure.[55]

In general, the SCAN-based functionals predict smaller interlayer distances than the corresponding PBE-based functionals, suggesting tighter binding of the underlying crystal structures. This is consistent with previous studies which compared *c* lattice parameter predictions of PBE and SCAN for layered $LiNiO_2$ and $LiCoO_2$.[49] Additionally, including rVV10 with SCAN or SCAN+*U* results in a marginally lower *c* parameter, while adding D3 to PBE or PBE+*U* does not necessarily lead to a lower *c* parameter, as observed in $LiVO_2$ and $LiCuO_2$. Also, SCAN-based functionals do not exceed the experimental *c* parameter value (except marginally in $LiNiO_2$), while at least one of the PBE-based functionals exceeds the experimental value for all systems, suggesting a systematic improvement in obtained lattice parameters with SCAN-based compared to PBE-based functionals. Overall, the calculated interlayer spacings from all functionals vary marginally, with the maximum error (in $LiVO_2$) being < 5% compared to the experimental value. This is expected, since the MO_2 layers are bound via strong Li-O electrostatic interactions; the much weaker long-range dispersion forces should have little effect on the structure.

Layered $LiMO_2$ cathode materials charge and discharge via de-lithiation and lithiation, respectively. Hence, we also examine the calculated interlayer distances for de-lithiated MO_2. **Figure 3** plots the calculated *c* lattice parameters for the seven fully de-lithiated MO_2 systems

View Article Online
DOI: 10.1039/D1CP03163E

considered, with notations similar to **Figure 2**. We consider the O1-type layered structure for CoO_2, which has been observed to form upon de-lithiation of layered O3-$LiCoO_2$.[56] In the case of NiO_2, all XC models except PBE predict the $R\bar{3}mH$ (O3) structure that is available in the ICSD to be more stable by 1-11 meV/f.u. than the $C2/m$ (O1). Notably, PBE predicts O1-NiO_2 to be more stable than O3-NiO_2 by only ~2 meV/f.u. Hence, we have displayed the interlayer spacings of O3-NiO_2 in **Figure 3**. For the remaining MO_2 systems that do not have reliable experimental structures, we constructed the MO_2 structures by removing the Li atoms from the corresponding $LiMO_2$ structures, followed by a full structure relaxation using each of the eight XC models.

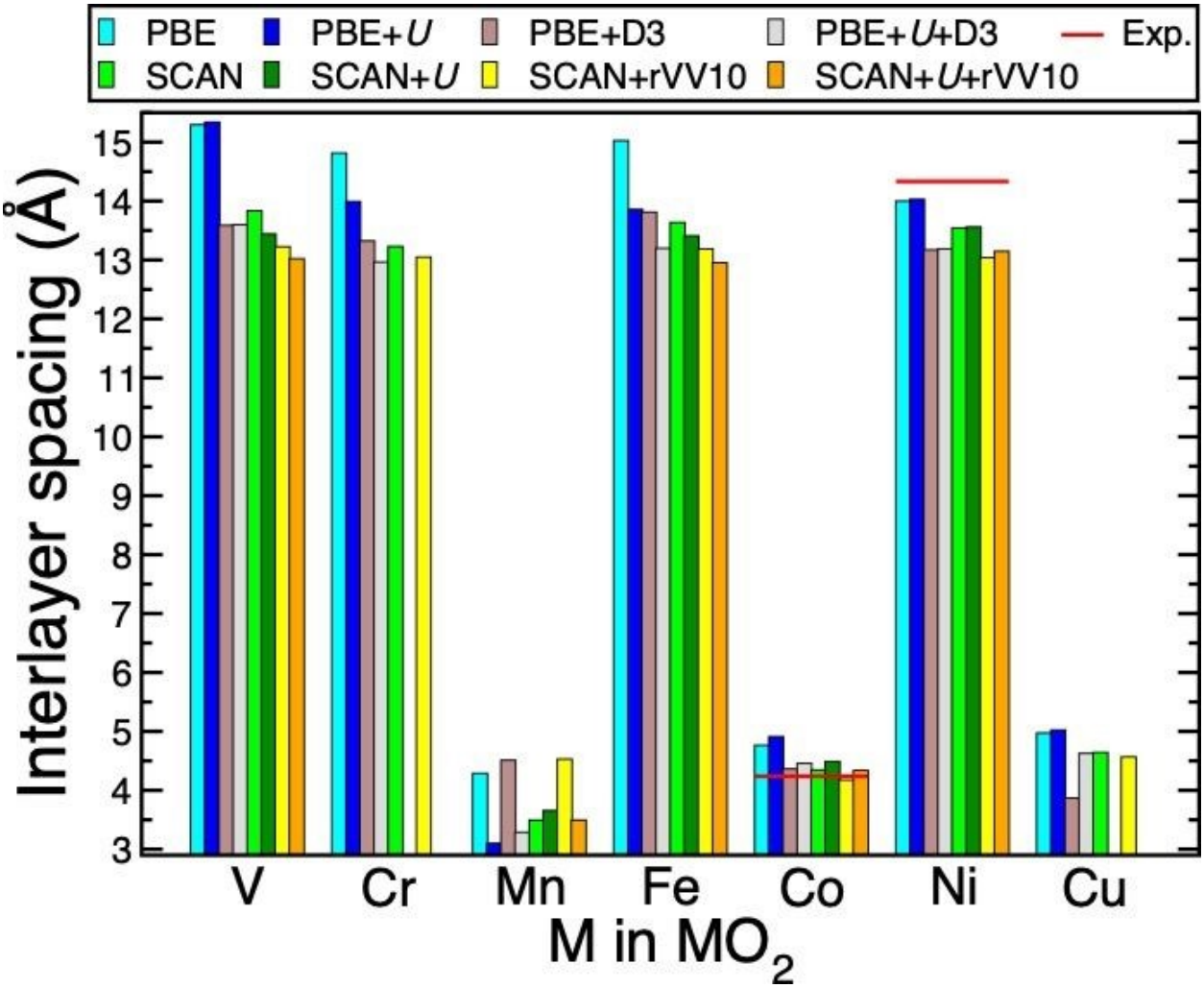

Figure 3: Interlayer spacing (c lattice parameter) predicted by the various XC models in the seven fully de-lithiated

View Article Online
DOI: 10.1039/D1CP03163E

MO_2 systems considered. The notations in this figure are similar to those of **Figure 2**. MnO_2, CoO_2, and CuO_2 have a single M layer in their structure while the other oxides exhibit three M layers.

Similar to the trend in the $LiMO_2$ systems, SCAN-based functionals generally predict smaller interlayer distances in MO_2. Furthermore, the change in layer spacing upon adding dispersion corrections is less significant for SCAN(+*U*), across the MO_2 systems (on the order of 0.5 Å or less, except MnO_2), than for PBE(+*U*) (more than 0.5 Å in several systems, with the largest deviation being ~1.7 Å in VO_2). This confirms that SCAN appears to capture the short-range and intermediate-range nonbonded interactions better than PBE, as claimed in the original work of Perdew and coworkers.[18] **Figure 3** also shows that the trends in spacing are more systematic with SCAN than with PBE, i.e., variations in layer spacing between the SCAN-based functionals are smaller than between PBE-based functionals (again with the exception of MnO_2). The large variations in *c* parameters, both by PBE- and SCAN-based functionals in de-lithiated MnO_2 is likely due to the transition from a Jahn-Teller distorted structure of $LiMnO_2$ to a non-distorted structure upon Li removal. Using available experimental data, we find that SCAN-based functionals better predict the interlayer spacing in CoO_2 compared to PBE-based ones. For NiO_2, both SCAN-based and PBE-based functionals underestimate the interlayer spacing, which may be due to inaccurate experimental values arising from residual Li in the structure.[57] However, more experimental data are needed to determine whether SCAN or PBE performs better in modeling the structural properties of MO_2 systems.

Topotactic Voltages

Figure 4 plots the calculated average topotactic voltages (**Eq. 1**), versus Li metal, for each of the $LiMO_2/MO_2$ systems. Green symbols indicate SCAN-based functionals and orange markers

View Article Online
DOI: 10.1039/D1CP03163E

indicate PBE-based functionals. The functional variant (e.g. SCAN+*U*, PBE+D3, etc.) is depicted by the shape and filling of the marker. Experimental voltage data (indicated by solid red lines[4,47,58–61]) are not available for the Cr, Fe, and Cu systems (i.e., the average voltages for the entire $LiMO_2$-MO_2 range are unavailable).

We find that SCAN-based models generally predict larger average voltages than the corresponding PBE-based ones (green vs. orange in **Figure 4**). Adding van der Waals corrections to PBE or PBE+*U* increases the predicted voltage in both cases (filled/empty circles vs. filled/empty squares in **Figure 4**). However, the change in voltage upon addition of rVV10 to SCAN(+*U*) is much smaller than when adding D3 to PBE(+*U*). This supports the claim that SCAN captures more of the dispersion interactions than PBE. Moreover, the effect of adding *U* corrections on voltage estimates is consistently larger for PBE-based functionals than for SCAN-based functionals (filled vs. empty symbols), probably because of the larger *U* values required for PBE[23] and the larger magnitude of the self-interaction errors within PBE.[27]

View Article Online
DOI: 10.1039/D1CP03163E

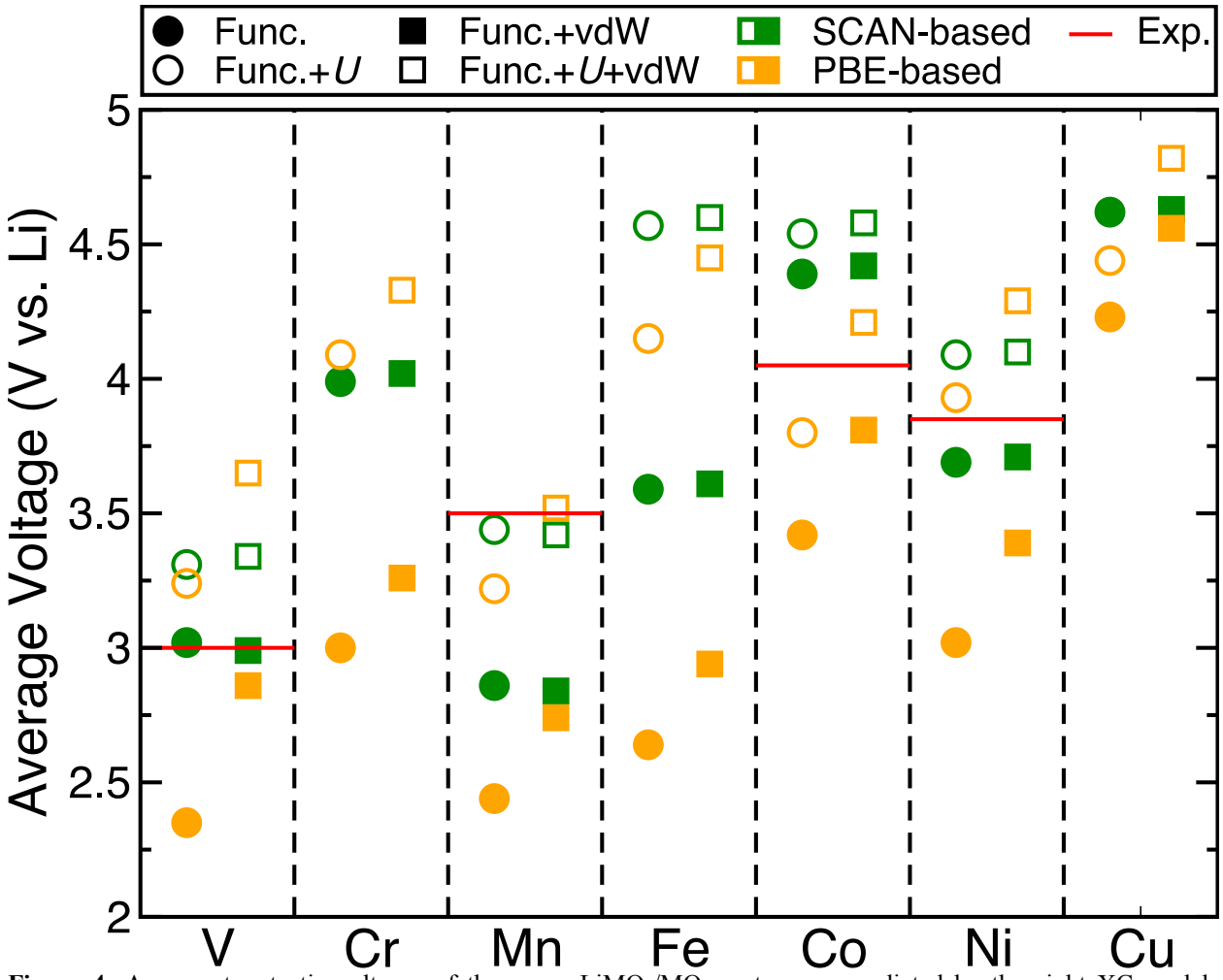

Figure 4: Average topotactic voltages of the seven $LiMO_2/MO_2$ systems as predicted by the eight XC models considered in this work. Green (orange) symbols indicates SCAN(PBE)-based functionals. Shape and filling of the marker indicate the type of the functional variant used. Red lines are experimental values. Cr and Cu do not have SCAN+*U* or SCAN+*U*+rVV10 values since no *U* correction is needed.

Using available experimental data, we find that SCAN+*U*(+rVV10) and PBE+*U*+D3 better agree with the measured voltage for Mn and Co, while PBE+*U* best estimates the voltage for the Ni system. For V, we observe that SCAN predicts the average voltage in closest agreement with experiment. However, this is purely coincidental, since V is known to require a *U* correction within the SCAN+*U* framework.[27] Notably, all SCAN-based functionals capture the expected voltage drop from $LiCoO_2$ to $LiNiO_2$, which occurs due to the addition of an electron (per metal ion) to the unfilled, antibonding e_g band in NiO_2.[47] By contrast, PBE+*U* and PBE+*U*+D3 unphysically predict higher voltages for $LiNiO_2$ than for $LiCoO_2$, even though PBE+*U*'s magnitude of error in

View Article Online
DOI: 10.1039/D1CP03163E

voltage predicted for $LiCoO_2$ and $LiNiO_2$ is lower than that of SCAN+*U*. This indicates that PBE+*U*'s precise voltage predictions are not due to the correct physics. Also, the *U* correction for Ni that is typically used with PBE (~5-6 eV) is often significantly higher than the one used for Co (~3-4 eV),[26,62–65] possibly explaining the inaccurate voltage trends of PBE+*U*.

Stability

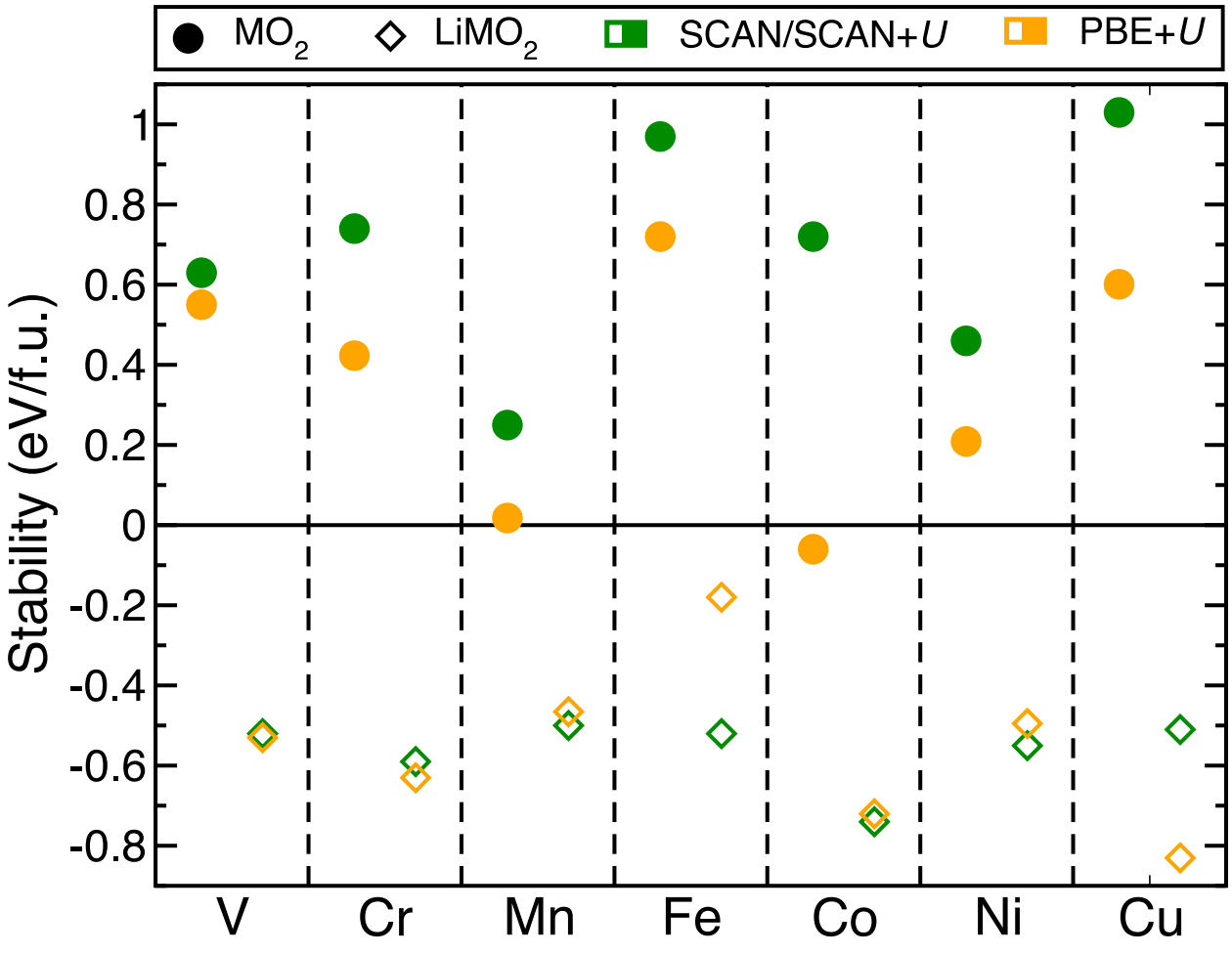

Figure 5: Predicted stabilities (see **Eqs. 2-10**) for $LiMO_2$ (diamonds) and MO_2 (circles) using SCAN(+*U*) and PBE+*U*. Green and orange symbols indicate SCAN(+*U*) and PBE+*U*, respectively.

The average voltage in a given intercalation system can increase by lowering the energy (i.e., increasing stability) of $LiMO_2$ and/or raising the energy of MO_2 (i.e., decreasing stability). Thus, to investigate the systematic larger voltages calculated by SCAN-based functionals, we computed

View Article Online
DOI: 10.1039/D1CP03163E

the stabilities of the $LiMO_2$ (diamonds) and MO_2 (circles) systems, using PBE- (orange symbols) and SCAN-based (green symbols), as shown in **Figure 5.** Positive (negative) stability values in **Figure 5** indicate increasing instability (stability) of a given compound, against its competing phases (see **Methods**). In case of Cr and Cu systems, we calculated the stabilities using SCAN instead of SCAN+*U*, since no *U* correction is needed.[27]

Importantly, we find that SCAN(+*U*) consistently predicts higher energies for the metastable, layered-MO_2 phases when compared to PBE+*U*. The differences in predicted stabilities for $LiMO_2$ are generally not significant (< 0.3 eV/f.u.), with the exception of $LiCoO_2$ and $LiCuO_2$. Thus, the higher voltages predicted by SCAN-based functionals can be attributed to the larger instabilities (higher energies) of MO_2. However, more experimental data are needed to determine whether SCAN(+*U*) or PBE+*U* is better at predicting accurate phase stabilities and the magnitude of instabilities, particularly for the metastable, layered-MO_2 systems. Since PBE+*U* data on the $LiMO_2$/MO_2 systems and their competing phases were available from the Materials Project,[44] we compared stabilities only between SCAN(+*U*) and PBE+*U*. Thus, further work is needed to evaluate the stability predictions after adding van der Waals corrections. However, we do not expect significant changes to the larger predicted instabilities of layered MO_2 when using SCAN(+*U*)+rVV10, since the predicted average voltages do not change significantly with the rVV10 addition.

View Article Online
DOI: 10.1039/D1CP03163E

Band gaps

Table 1: Band gaps (eV) from measurements and calculated using SCAN- and PBE-based XC models for all $LiMO_2$ and MO_2 compositions considered in this work. Columns indicate the type of XC model used. All eight models predict metallic (or half-metallic) behavior in VO_2, CrO_2, MnO_2, FeO_2, and CuO_2 and experimental band gaps are not available for any of these layered oxides. For NiO_2, we list band gaps for both the O3 ($R\bar{3}mH$) and O1 ($C2/m$) structures.

Composition (space group)	Band gap (eV)				
	Source	Functional	Functional + U	Functional + vdW	Functional + U + vdW
$LiVO_2$ ($R\bar{3}mH$)	SCAN	0	0.548	0	0.528
	PBE	0	1.463	0	1.443
	Experiment	0.18[66]			
$LiCrO_2$ ($R\bar{3}mH$)	SCAN	0.983	N/A	0.943	N/A
	PBE	0.698	2.783	0.593	2.833
	Experiment	1.81 – 2.48 eV[67]			
$LiMnO_2$ ($C12/m1$)	SCAN	0.377	1.327	0.342	1.307
	PBE	0.302	0.977	0.137	1.012
	Experiment	Semiconductor[68]			
$LiFeO_2$ ($R\bar{3}mH$)	SCAN	0.163	1.473	0.148	1.448
	PBE	0	1.098	0	1.043
	Experiment	Insulator[69]			
$LiCoO_2$ ($R\bar{3}mH$)	SCAN	0.871	3.067	0.876	3.067
	PBE	0.831	2.027	0.881	2.072
	Experiment	2.7±0.3[70]			
$LiNiO_2$ ($C2/m$)	SCAN	0	0.147	0	0.147
	PBE	0	0.022	0	0.107
	GGA+U+G_0W_0[a]	~ 0.96[71]			
$LiCuO_2$ ($C12/m1$)	SCAN	0.246	N/A	0.221	N/A
	PBE	0.121	0.346	0.136	0.351
	Experiment	Semiconductor[72]			
CoO_2 ($P\bar{3}m1$)	SCAN	0	1.476	0	1.341
	PBE	0	1.116	0	0.896
	Experiment	Pauli paramagnetic metal[73]			
O3-NiO_2 ($R\bar{3}mH$)	SCAN	0.746	1.482	0.656	1.371
	PBE	0.721	1.167	0.631	0.986
O1-NiO_2 ($C2/m$)	SCAN	0.686	1.402	0.646	1.337
	PBE	0.746	1.187	0.616	0.962
	GGA+U+G_0W_0[a]	2.22[71]			

[a]Used as a proxy for experimental data

Band (KS eigenvalue) gaps for the seven $LiMO_2$ systems, CoO_2, and NiO_2 calculated using the eight XC models considered are shown in **Table 1** along with available experimental data. All XC models predict metallic (or half-metallic) behavior in de-lithiated VO_2, CrO_2, MnO_2, FeO_2, and

View Article Online
DOI: 10.1039/D1CP03163E

CuO_2 structures, where there are no experimental band gaps to compare against. For the O1 structures of $LiNiO_2$ and NiO_2, we use a GGA+*U*+G_0W_0 quasiparticle band gap from a previous study[71] as a proxy for experimental data, since single-shot G_0W_0 calculations generally predict band gaps accurately.[74–78] Also, we include calculated band gaps for both the O1 ($C2/m$) and O3 ($R\bar{3}mH$) structures of NiO_2 in **Table 1**, with no experimental or G_0W_0 data available to benchmark the band gap of the O3 structure.

We find that SCAN+*U*(+rVV10) and PBE+*U*(+D3) functionals qualitatively agree with available measurements in $LiMO_2$ systems. Specifically, all $LiMO_2$ systems are calculated to be non-metallic by SCAN+*U*(+rVV10) and PBE+*U*(+D3), which agrees with experimental (or G_0W_0-calculated) observations. In the case of O1-NiO_2, all eight XC models agree qualitatively with the G_0W_0-calculated gap. Also, SCAN-based band gaps are generally larger, and in better quantitative agreement with experiments/G_0W_0, than the corresponding PBE-based band gaps, with $LiVO_2$ being the only exception (where SCAN+*U*(+rVV10) is again in better quantitative agreement with the experimental gap of 0.18 eV compared to PBE+*U*(+D3)). In any case, robust quantitative agreement (i.e., errors in the range of $\pm$ 0.1 eV) with experimental/G_0W_0 band gaps of $LiMO_2$ does not exist for any functional, which is expected given that regular DFT or its Hubbard *U* corrected variants are (typically) not designed to predict accurate band gaps.[17,27,46]

For the case of CoO_2, both SCAN+*U*(+rVV10) and PBE+*U*(+D3) predict a qualitatively wrong semiconducting behavior compared to experiments. Moreover, adding van der Waals corrections to both SCAN+*U* and PBE+*U* only results in a marginal reduction (~0.14-0.22 eV) of the predicted band gap in CoO_2. The qualitative disagreement of the predicted electronic structure in CoO_2 by both SCAN+*U*(+rVV10) and PBE+*U*(+D3) can be attributed to the general failure of DFT+*U* theory in modeling metallic systems, as alluded to in our previous study.[27]

View Article Online
DOI: 10.1039/D1CP03163E

Importantly, for each functional variant (columns of **Table 1**), both SCAN-based and PBE-based functionals predict the same qualitative behavior in both $LiMO_2$ and MO_2 (i.e., if SCAN(+*U*+rVV10) predicts a material to be metallic, PBE(+*U*+D3) does as well). Such qualitative agreement is useful in cross-validating various theoretical approximations, especially for band gap calculations in systems with scarce data. The only exception to this qualitative agreement is $LiFeO_2$, where SCAN(+rVV10) predicts semiconducting behavior in contrast to PBE(+D3). Our data thus indicates that using SCAN-based functionals for layered TMOs does not result in any dramatic improvement in either qualitative or quantitative band gap predictions compared to the corresponding PBE-based counterparts.

View Article Online
DOI: 10.1039/D1CP03163E

Electronic structure in select systems

In this section, we analyze the calculated electronic structures in a few select systems to highlight the similarities and differences among the eight XC models used in this work.

$LiMnO_2$

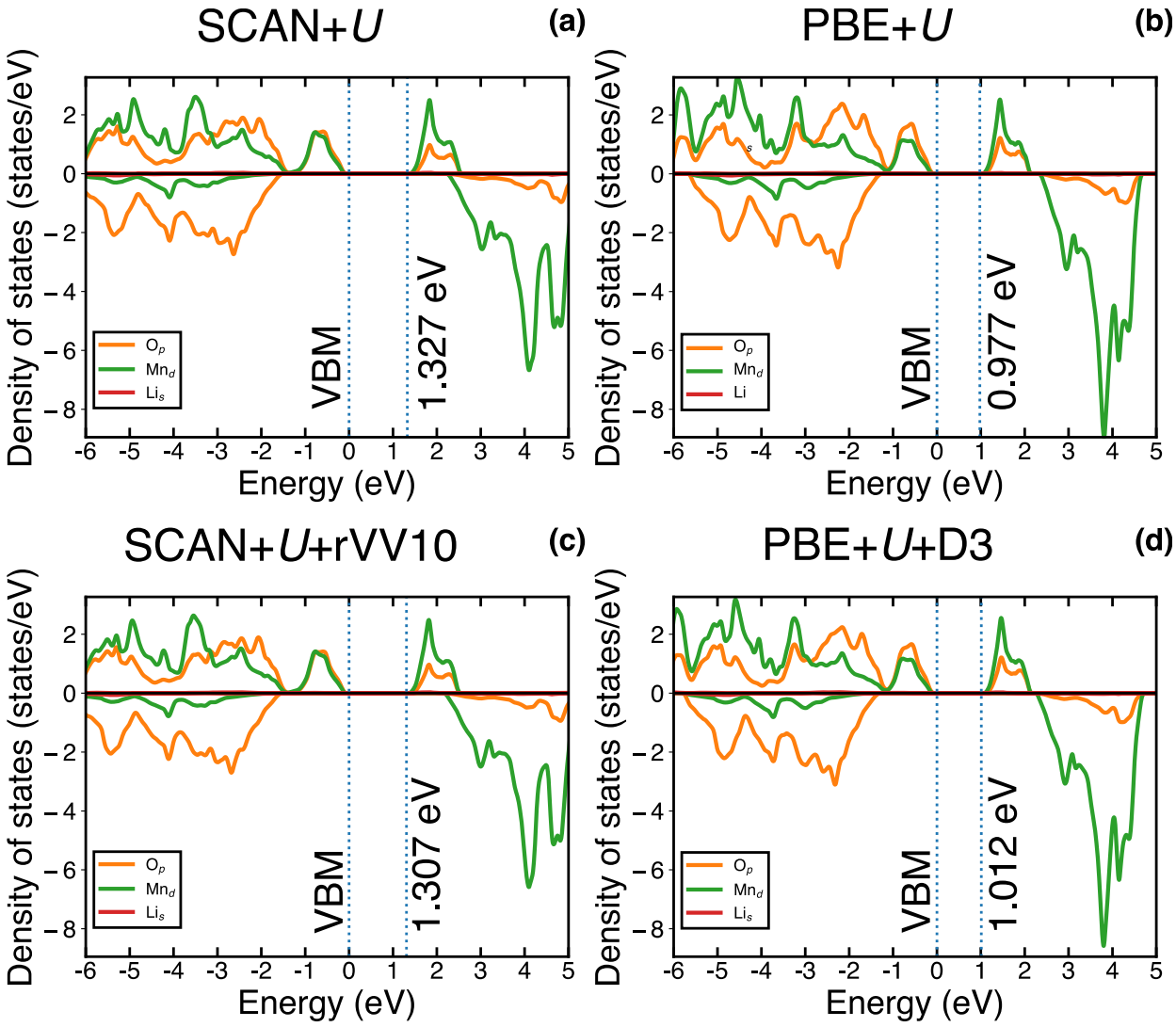

Figure 6: Density of states (DOS) for $LiMnO_2$ $(C12/m1)$ as calculated by (a) SCAN+U, (b) PBE+U, (c) SCAN+U+rVV10, and (d) PBE+U+D3 where $U = 2.7$ eV for SCAN and $U = 3.9$ eV for PBE. Orange, green, and red curves correspond to O 2p, transition metal (Mn) 3d, and Li 2s states, respectively. Dotted blue lines are valence and conduction band edges. The zero on the energy scale is set to the valence band maximum (VBM), with the KS band gap indicated by the text annotation at the conduction band minimum (CBM). States/eV plotted as negative (positive) are minority (majority) spin.

View Article Online
DOI: 10.1039/D1CP03163E

Figure 6 plots the density of states (DOS) predicted by SCAN+*U,* PBE+*U*, SCAN+*U*+rVV10, and PBE+*U*+D3, where *U* is 2.7 eV with SCAN and 3.9 eV with PBE. As shown in **Table 1**, we observe that SCAN-based functionals predict larger band gaps than the corresponding PBE-based functionals. For example, SCAN+*U* predicts a higher band gap of 1.327 eV compared to the 0.977 eV predicted by PBE+*U*. Likewise, SCAN+*U*+rVV10 predicts a 1.307 eV band gap, while PBE+*U*+D3 predicts a band gap of 1.012 eV. Moreover, all four XC models predict the valence band edges to be a mixture of Mn 3*d* and O 2*p* states, while the conduction band edges are largely dominated by Mn 3*d* states. Comparing **Figure 6a** and **Figure 6c**, we also find that adding the van der Waals corrections to SCAN+*U* results in a ~1.5% decrease in the calculated band gap value. On the other hand, the band gap increases by ~4% for PBE+*U* (**Figures 6b, d**). Thus, adding dispersion corrections has little effect on the band gap predictions for Hubbard *U* corrected SCAN and PBE, albeit in qualitatively different directions.

$LiCoO_2$

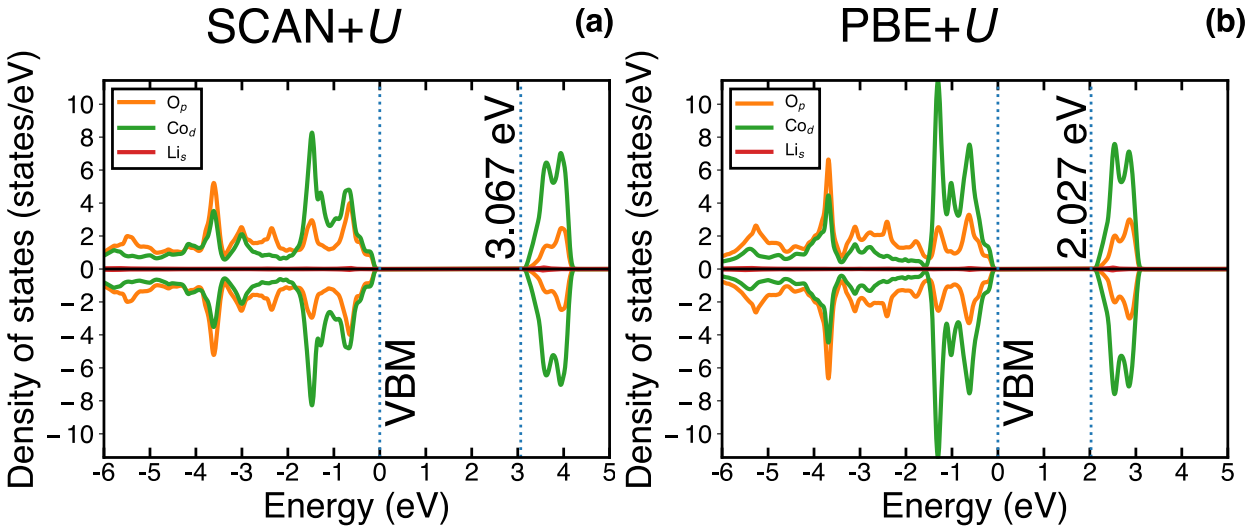

Figure 7: DOS for $LiCoO_2$ as calculated by (a) SCAN+*U* (*U* = 3.0 eV) and (b) PBE+*U* (*U* = 3.4 eV). Notations used within each panel are identical to **Figure 6**.

View Article Online
DOI: 10.1039/D1CP03163E

$LiCoO_2$ is an insulator with a measured band gap of 2.7 ± 0.3 eV.[70] The DOS in **Figure 7** suggest that SCAN+*U* (*U* = 3.0 eV) very slightly overestimates the band gap, predicting a value of 3.067 eV, while PBE+*U* (*U* = 3.4 eV) predicts a much lower band gap of 2.027 eV. Both SCAN+*U* and PBE+*U* predict similar distributions of Co 3*d* and O 2*p* states at the valence band edge (with SCAN+*U* predicting a larger proportion of O 2*p* than PBE+*U*) and Co 3*d* states at the conduction band edge. Adding dispersion corrections did not yield significantly different band gaps for either PBE+*U* or SCAN+*U* (**Table 1**), consistent with general trends observed over all $LiMO_2$ and MO_2 systems. Dispersion corrections only indirectly alter band gaps through geometric structural changes; hence the minor changes upon adding dispersion.

$LiFeO_2$

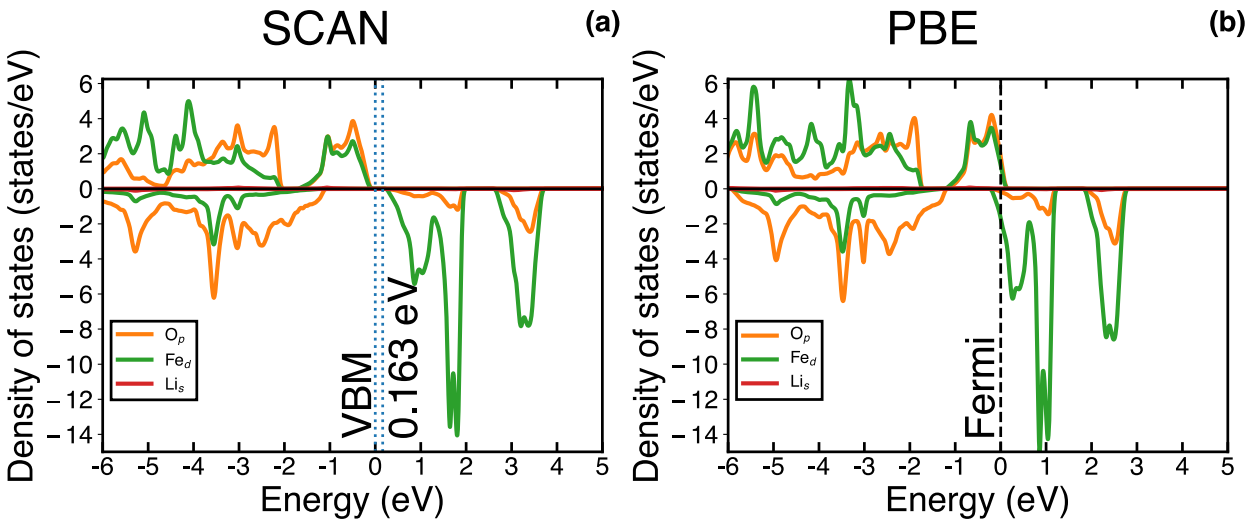

Figure 8: DOS for $LiFeO_2$ as calculated by (a) SCAN and (b) PBE. The dashed black line in panel (b) indicates the Fermi level, which is also used as the reference for the energy axis. Notations used within each panel are similar to **Figure 6**.

Of the seven $LiMO_2$ systems considered, $LiFeO_2$ is the only case where the predicted electronic behavior differs qualitatively between SCAN(+rVV10) and PBE(+D3). **Figure 8** depicts the DOS predicted by SCAN and PBE, in panels a and b, respectively. Experimentally, $LiFeO_2$ is known to be a charge-transfer insulator.[69] SCAN correctly predicts a band gap whereas PBE predicts

View Article Online
DOI: 10.1039/D1CP03163E

metallic behavior. Moreover, SCAN captures the charge-transfer behavior, since there are similar numbers of O 2*p* and Fe 3*d* states near the VBM compared to the predominantly Fe 3*d* states near the CBM. This qualitative difference in electronic structure is the likely source for the stability differences observed between SCAN and PBE (**Figure 5**), since SCAN predicts a larger stability (lower relative energy) compared to PBE.

Conclusion

Given the importance of layered 3*d* transition-metal oxides in energy (particularly battery) applications, we assessed the ability of SCAN(+*U*) and PBE(+*U*) functionals, with and without dispersion corrections, to predict structural, electrode (average voltages), thermodynamic (stability), and electronic (band gap) properties of layered $LiMO_2$ and de-lithiated MO_2 phases. PBE(+*U*) functionals have been used widely in computational studies of battery electrode materials while SCAN(+*U*) had not been benchmarked extensively prior to this work, particularly in layered transition-metal oxides. We found that both SCAN- and PBE-based functionals perform well in predicting interlayer spacings in $LiMO_2$ and MO_2. Generally, SCAN-based functionals predicted smaller interlayer spacings in these materials compared those arising from the corresponding PBE-based functionals. SCAN tends to predict higher topotactic voltages than PBE due to SCAN underestimating the stability of de-lithiated MO_2 in each Li-M-O system. Despite its frequent overprediction of voltages, SCAN+*U* does capture correctly the qualitative trend of the dip in average voltage going from $LiCoO_2$ to $LiNiO_2$. Importantly, adding dispersion corrections did not (did) affect layer spacings and voltage predictions of SCAN(+*U*) (PBE(+*U*)) significantly, supporting the hypothesis that SCAN captures short- and medium-range van der Waals interactions better than PBE. However, more experimental data are needed to determine conclusively which functional better predicts voltages and stabilities. In any case, the frequent

View Article Online
DOI: 10.1039/D1CP03163E

overestimation of average intercalation voltages should be factored into any future theoretical studies of battery electrodes using SCAN+*U*.

Both SCAN+*U*(+rVV10) and PBE+*U*(+D3) correctly predict qualitative aspects of the electronic structure of $LiMO_2$ and MO_2 systems, with the exception of de-lithiated CoO_2. The addition of van der Waals corrections only marginally affected band gap predictions by SCAN- and PBE-based functionals. Indeed, even in de-lithiated systems such as CoO_2 and NiO_2, adding van der Waals corrections did not change band gaps by more than ~0.2 eV, indicating the negligible impact of dispersion corrections on band gaps. SCAN-based functionals are in only slightly better quantitative agreement than corresponding PBE-based functionals with available experimental electronic structure data, suggesting that SCAN-based functionals do not offer a significant improvement over PBE-based functionals in terms of electronic structure predictions for layered TMOs. However, SCAN-based functionals do provide better systematic trends in band gaps, interlayer spacings, and average voltages. Hence, given the stronger theoretical underpinning of SCAN vs. PBE, we expect SCAN(+*U*) to yield better property predictions compared to PBE(+*U*) in most TMO systems.

Conflicts of interest

There are no conflicts of interest to declare.

Acknowledgments

E.A.C. thanks the U.S. Department of Energy, Office of Energy Efficiency and Renewable Energy, under Award No. DE-EE0008090 for funding this project. O.L. acknowledges financial support from the Princeton Office of Undergraduate Research. The authors thank Princeton Research Computing resources at Princeton University, a consortium of groups including the Princeton Institute for Computational Science and Engineering and the Princeton University Office of

View Article Online
DOI: 10.1039/D1CP03163E

Information Technology's Research Computing department. The authors also acknowledge computational resources sponsored by the Department of Energy's Office of Energy Efficiency and Renewable Energy located at the National Renewable Energy Laboratory.

References

1 M. S. Whittingham, Lithium batteries and cathode materials, *Chem. Rev.*, 2004, **104**, 4271–4302.
2 M. S. Whittingham, Ultimate Limits to Intercalation Reactions for Lithium Batteries, *Chem. Rev.*, 2014, **114**, 11414–11443.
3 J. B. Goodenough and K.-S. Park, The Li-Ion Rechargeable Battery: A Perspective, *J. Am. Chem. Soc.*, 2013, **135**, 1167–1176.
4 T. Ohzuku and A. Ueda, Why transition metal (di) oxides are the most attractive materials for batteries, *Solid State Ionics*, 1994, **69**, 201–211.
5 Y. Ding, Z. P. Cano, A. Yu, J. Lu and Z. Chen, Automotive Li-Ion Batteries: Current Status and Future Perspectives, *Electrochem. Energy Rev.*, 2019, **2**, 1–28.
6 J. Liu, J.-G. Zhang, Z. Yang, J. P. Lemmon, C. Imhoff, G. L. Graff, L. Li, J. Hu, C. Wang, J. Xiao, G. Xia, V. V. Viswanathan, S. Baskaran, V. Sprenkle, X. Li, Y. Shao and B. Schwenzer, Materials Science and Materials Chemistry for Large Scale Electrochemical Energy Storage: From Transportation to Electrical Grid, *Adv. Funct. Mater.*, 2013, **23**, 929–946.
7 J. E. Harlow, X. Ma, J. Li, E. Logan, Y. Liu, N. Zhang, L. Ma, S. L. Glazier, M. M. E. Cormier, M. Genovese, S. Buteau, A. Cameron, J. E. Stark and J. R. Dahn, A Wide Range of Testing Results on an Excellent Lithium-Ion Cell Chemistry to be used as Benchmarks for New Battery Technologies, *J. Electrochem. Soc.*, 2019, **166**, A3031–A3044.
8 P. Canepa, G. Sai Gautam, D. C. Hannah, R. Malik, M. Liu, K. G. Gallagher, K. A. Persson and G. Ceder, Odyssey of Multivalent Cathode Materials: Open Questions and Future Challenges, *Chem. Rev.*, 2017, **117**, 4287–4341.
9 M. Armand and J.-M. Tarascon, Building better batteries, *Nature*, 2008, **451**, 652–657.
10 J. B. Goodenough and Y. Kim, Challenges for Rechargeable Li Batteries, *Chem. Mater.*, 2010, **22**, 587–603.
11 B. Dunn, H. Kamath and J.-M. Tarascon, Electrical Energy Storage for the Grid: A Battery of Choices, *Science (80-.).*, 2011, **334**, 928–935.
12 U.-H. Kim, D.-W. Jun, K.-J. Park, Q. Zhang, P. Kaghazchi, D. Aurbach, D. T. Major, G. Goobes, M. Dixit, N. Leifer, C. M. Wang, P. Yan, D. Ahn, K.-H. Kim, C. S. Yoon and Y.-K. Sun, Pushing the limit of layered transition metal oxide cathodes for high-energy density rechargeable Li ion batteries, *Energy Environ. Sci.*, 2018, **11**, 1271–1279.
13 A. Manthiram, A reflection on lithium-ion battery cathode chemistry, *Nat. Commun.*, 2020, **11**, 1550.
14 P. Hohenberg and W. Kohn, Inhomogeneous Electron Gas, *Phys. Rev.*, 1964, **136**, B864–B871.
15 W. Kohn and L. J. Sham, Self-Consistent Equations Including Exchange and Correlation Effects, *Phys. Rev.*, 1965, **140**, A1133–A1138.
16 J. P. Perdew and A. Zunger, Self-interaction correction to density-functional approximations for many-electron systems, *Phys. Rev. B*, 1981, **23**, 5048–5079.
17 J. P. Perdew, in *Advances in Quantum Chemistry*, ed. P.-O. Lōwdin, Academic Press, 1990, pp. 113–134.
18 J. Sun, A. Ruzsinszky and J. P. Perdew, Strongly Constrained and Appropriately Normed Semilocal Density Functional, *Phys. Rev. Lett.*, 2015, **115**, 036402.
19 J. P. Perdew, K. Burke and M. Ernzerhof, Generalized Gradient Approximation Made Simple, *Phys. Rev. Lett.*, 1996, **77**, 3865–3868.
20 N. Alidoust and E. A. Carter, First-principles assessment of hole transport in pure and Li-doped

View Article Online
DOI: 10.1039/D1CP03163E

NiO, *Phys. Chem. Chem. Phys.*, 2015, **17**, 18098–18110.
21 A. M. Ritzmann, A. B. Muñoz-García, M. Pavone, J. A. Keith and E. A. Carter, Ab Initio DFT+U Analysis of Oxygen Vacancy Formation and Migration in La1-xSrxFeO3-δ (x = 0, 0.25, 0.50), *Chem. Mater.*, 2013, **25**, 3011–3019.
22 P. Liao and E. A. Carter, Hole transport in pure and doped hematite, *J. Appl. Phys.*, 2012, **112**, 013701.
23 G. Sai Gautam and E. A. Carter, Evaluating transition metal oxides within DFT-SCAN and SCAN+U frameworks for solar thermochemical applications, *Phys. Rev. Mater.*, 2018, **2**, 095401.
24 V. I. Anisimov, J. Zaanen and O. K. Andersen, Band theory and Mott insulators: Hubbard U instead of Stoner I, *Phys. Rev. B*, 1991, **44**, 943–954.
25 V. I. Anisimov, F. Aryasetiawan and A. I. Lichtenstein, First-principles calculations of the electronic structure and spectra of strongly correlated systems: the LDA + U method, *J. Phys. Condens. Matter*, 1997, **9**, 767–808.
26 L. Wang, T. Maxisch and G. Ceder, Oxidation energies of transition metal oxides within the GGA + U framework, *Phys. Rev. B*, 2006, **73**, 195107.
27 O. Y. Long, G. Sai Gautam and E. A. Carter, Evaluating optimal U for 3d transition-metal oxides within the SCAN+U framework, *Phys. Rev. Mater.*, 2020, **4**, 045401.
28 F. Tran, L. Kalantari, B. Traoré, X. Rocquefelte and P. Blaha, Nonlocal van der Waals functionals for solids: Choosing an appropriate one, *Phys. Rev. Mater.*, 2019, **3**, 063602.
29 Y. Zhao and D. G. Truhlar, Comparative DFT Study of van der Waals Complexes: Rare-Gas Dimers, Alkaline-Earth Dimers, Zinc Dimer, and Zinc-Rare-Gas Dimers, *J. Phys. Chem. A*, 2006, **110**, 5121–5129.
30 M. S. Whittingham, Intercalation chemistry and energy storage, *J. Solid State Chem.*, 1979, **29**, 303–310.
31 S. Grimme, J. Antony, S. Ehrlich and H. Krieg, A consistent and accurate ab initio parametrization of density functional dispersion correction (DFT-D) for the 94 elements H-Pu, *J. Chem. Phys.*, 2010, **132**, 154104–19.
32 R. O. Jones, Density functional theory: Its origins, rise to prominence, and future, *Rev. Mod. Phys.*, 2015, **87**, 897–923.
33 R. Car, Density functional theory: Fixing Jacob's ladder, *Nat. Chem.*, 2016, **8**, 820–821.
34 H. Peng, Z.-H. Yang, J. P. Perdew and J. Sun, Versatile van der Waals Density Functional Based on a Meta-Generalized Gradient Approximation, *Phys. Rev. X*, 2016, **6**, 041005.
35 O. A. Vydrov and T. Van Voorhis, Nonlocal van der Waals density functional: The simpler the better, *J. Chem. Phys.*, 2010, **133**, 244103.
36 R. Sabatini, T. Gorni and S. de Gironcoli, Nonlocal van der Waals density functional made simple and efficient, *Phys. Rev. B*, 2013, **87**, 041108.
37 G. Kresse and J. Hafner, Ab initio molecular dynamics for liquid metals, *Phys. Rev. B*, 1993, **47**, 558–561.
38 G. Kresse and J. Furthmüller, Efficient iterative schemes for ab initio total-energy calculations using a plane-wave basis set, *Phys. Rev. B*, 1996, **54**, 11169–11186.
39 G. Kresse and D. Joubert, From ultrasoft pseudopotentials to the projector augmented-wave method, *Phys. Rev. B*, 1999, **59**, 1758–1775.
40 P. E. Blöchl, Projector augmented-wave method, *Phys. Rev. B*, 1994, **50**, 17953–17979.
41 H. J. Monkhorst and J. D. Pack, Special points for Brillouin-zone integrations, *Phys. Rev. B*, 1976, **13**, 5188–5192.
42 K.-M. Ho, C. L. Fu, B. N. Harmon, W. Weber and D. R. Hamann, Vibrational Frequencies and Structural Properties of Transition Metals via Total-Energy Calculations, *Phys. Rev. Lett.*, 1982, **49**, 673–676.
43 S. L. Dudarev, G. A. Botton, S. Y. Savrasov, C. J. Humphreys and A. P. Sutton, Electron-energy-loss spectra and the structural stability of nickel oxide: An LSDA+U study, *Phys. Rev. B*, 1998, **57**, 1505–1509.

View Article Online
DOI: 10.1039/D1CP03163E

44 A. Jain, S. P. Ong, G. Hautier, W. Chen, W. D. Richards, S. Dacek, S. Cholia, D. Gunter, D. Skinner, G. Ceder and K. A. Persson, Commentary: The Materials Project: A materials genome approach to accelerating materials innovation, *APL Mater.*, 2013, **1**, 011002.
45 M. Hellenbrandt, The Inorganic Crystal Structure Database (ICSD)—Present and Future, *Crystallogr. Rev.*, 2004, **10**, 17–22.
46 J. P. Perdew, W. Yang, K. Burke, Z. Yang, E. K. U. Gross, M. Scheffler, G. E. Scuseria, T. M. Henderson, I. Y. Zhang, A. Ruzsinszky, H. Peng, J. Sun, E. Trushin and A. Görling, Understanding band gaps of solids in generalized Kohn–Sham theory, *Proc. Natl. Acad. Sci.*, 2017, **114**, 2801–2806.
47 M. K. Aydinol, A. F. Kohan and G. Ceder, Ab initio calculation of the intercalation voltage of lithium-transition-metal oxide electrodes for rechargeable batteries, *J. Power Sources*, 1997, **68**, 664–668.
48 N. Nitta, F. Wu, J. T. Lee and G. Yushin, Li-ion battery materials: Present and future, *Mater. Today*, 2015, **18**, 252.
49 A. Chakraborty, M. Dixit, D. Aurbach and D. T. Major, Predicting accurate cathode properties of layered oxide materials using the SCAN meta-GGA density functional, *npj Comput. Mater.*, 2018, **4**, 60.
50 A. Van der Ven, Z. Deng, S. Banerjee and S. P. Ong, Rechargeable Alkali-Ion Battery Materials: Theory and Computation, *Chem. Rev.*, 2020, **120**, 6977–7019.
51 F. Meutzner, T. Nestler, M. Zschornak, P. Canepa, G. S. Gautam, S. Leoni, S. Adams, T. Leisegang, V. A. Blatov and D. C. Meyer, Computational analysis and identification of battery materials, *Phys. Sci. Rev.*, 2019, **4**, 20180044.
52 L. de Biasi, A. O. Kondrakov, H. Geßwein, T. Brezesinski, P. Hartmann and J. Janek, Between Scylla and Charybdis: Balancing Among Structural Stability and Energy Density of Layered NCM Cathode Materials for Advanced Lithium-Ion Batteries, *J. Phys. Chem. C*, 2017, **121**, 26163–26171.
53 Y. Shao-Horn, Structural Characterization of Layered LiMnO[sub 2] Electrodes by Electron Diffraction and Lattice Imaging, *J. Electrochem. Soc.*, 1999, **146**, 2404–2412.
54 A. Rougier, C. Delmas and A. V. Chadwick, Non-cooperative Jahn-Teller effect in LiNiO2: An EXAFS study, *Solid State Commun.*, 1995, **94**, 123–127.
55 R. Berger and L.-E. Tergenius, Room temperature synthesis and structural characterization of monoclinic LiCuO2 by X-ray and neutron diffraction, *J. Alloys Compd.*, 1994, **203**, 203–207.
56 G. G. Amatucci, J. M. Tarascon and L. C. Klein, CoO2, The End Member of the LixCoO2 Solid Solution, *J. Electrochem. Soc.*, 1996, **143**, 1114–1123.
57 A. Hirano, R. Kanno, Y. Kawamoto, Y. Takeda, K. Yamaura, M. Takano, K. Ohyama, M. Ohashi and Y. Yamaguchi, Relationship between non-stoichiometry and physical properties in LiNiO2, *Solid State Ionics*, 1995, **78**, 123–131.
58 M. E. Arroyo y de Dompablo, A. Van der Ven and G. Ceder, First-principles calculations of lithium ordering and phase stability on LixNiO2, *Phys. Rev. B*, 2002, **66**, 064112.
59 C. Delmas, M. Ménétrier, L. Croguennec, S. Levasseur, J. P. Pérès, C. Pouillerie, G. Prado, L. Fournès and F. Weill, Lithium batteries: a new tool in solid state chemistry, *Int. J. Inorg. Mater.*, 1999, **1**, 11–19.
60 L. A. De Picciotto, M. M. Thackeray and G. Pistoia, An electrochemical study of the systems Li1+/-xV2O4 and Li1-xVO2 (0<=x<=1), *Solid State Ionics*, 1988, **28–30**, 1364–1370.
61 A. R. Armstrong and P. G. Bruce, Synthesis of layered LiMnO2 as an electrode for rechargeable lithium batteries, *Nature*, 1996, **381**, 499–500.
62 A. Jain, G. Hautier, S. P. Ong, C. J. Moore, C. C. Fischer, K. A. Persson and G. Ceder, Formation enthalpies by mixing GGA and GGA + U calculations, *Phys. Rev. B*, 2011, **84**, 045115.
63 J. Chen and A. Selloni, First Principles Study of Cobalt (Hydr)oxides under Electrochemical Conditions, *J. Phys. Chem. C*, 2013, **117**, 20002–20006.
64 X. Shi, S. L. Bernasek and A. Selloni, Formation, Electronic Structure, and Defects of Ni

View Article Online
DOI: 10.1039/D1CP03163E

Substituted Spinel Cobalt Oxide: a DFT+U Study, *J. Phys. Chem. C*, 2016, **120**, 14892–14898.

65 J. Zaffran and M. C. Toroker, Metal-Oxygen Bond Ionicity as an Efficient Descriptor for Doped NiOOH Photocatalytic Activity, *ChemPhysChem*, 2016, **17**, 1630–1636.

66 W. Tian, M. F. Chisholm, P. G. Khalifah, R. Jin, B. C. Sales, S. E. Nagler and D. Mandrus, Single crystal growth and characterization of nearly stoichiometric LiVO2, *Mater. Res. Bull.*, 2004, **39**, 1319–1328.

67 H. I. Elsaeedy, Synthesis and Characterization of LiCrO2 Thin Films As Potential Cathode Material for Lithium Ion Batteries, *J. Electron. Mater.*, 2020, **49**, 282–289.

68 V. R. Galakhov, M. A. Korotin, N. A. Ovechkina, E. Z. Kurmaev, V. S. Gorshkov, D. G. Kellerman, S. Bartkowski and M. Neumann, Electronic structure of LiMnO2: X-ray emission and photoelectron spectra and band structure calculations, *Eur. Phys. J. B*, 2000, **14**, 281–286.

69 V. R. Galakhov, E. Z. Kurmaev, S. Uhlenbrock, M. Neumann, D. G. Kellerman and V. S. Gorshkov, Electronic structure of LiNiO2, LiFeO2 and LiCrO2: X-ray photoelectron and X-ray emission study, *Solid State Commun.*, 1995, **95**, 347.

70 J. van Elp, J. L. Wieland, H. Eskes, P. Kuiper, G. A. Sawatzky, F. M. F. de Groot and T. S. Turner, Electronic structure of CoO, Li-doped CoO, and LiCoO2, *Phys. Rev. B*, 1991, **44**, 6090–6103.

71 D.-H. Seo, A. Urban and G. Ceder, Calibrating transition-metal energy levels and oxygen bands in first-principles calculations: Accurate prediction of redox potentials and charge transfer in lithium transition-metal oxides, *Phys. Rev. B*, 2015, **92**, 115118.

72 F. J. Owens, Evidence of a phase transition in Cu-O chains of LiCuO2, *Phys. C Supercond. its Appl.*, 1999, **313**, 65–69.

73 T. Motohashi, T. Ono, Y. Sugimoto, Y. Masubuchi, S. Kikkawa, R. Kanno, M. Karppinen and H. Yamauchi, Electronic phase diagram of the layered cobalt oxide system LixCoO2, *Phys. Rev. B*, 2009, **80**, 165114.

74 N. Alidoust, M. C. Toroker and E. A. Carter, Revisiting Photoemission and Inverse Photoemission Spectra of Nickel Oxide from First Principles: Implications for Solar Energy Conversion, *J. Phys. Chem. B*, 2014, **118**, 7963–7971.

75 M. C. Toroker, D. K. Kanan, N. Alidoust, L. Y. Isseroff, P. Liao and E. A. Carter, First principles scheme to evaluate band edge positions in potential transition metal oxide photocatalysts and photoelectrodes, *Phys. Chem. Chem. Phys.*, 2011, **13**, 16644.

76 G. Sai Gautam, T. P. Senftle, N. Alidoust and E. A. Carter, Novel Solar Cell Materials: Insights from First-Principles, *J. Phys. Chem. C*, 2018, **122**, 27107–27126.

77 P. Liao and E. A. Carter, Testing variations of the GW approximation on strongly correlated transition metal oxides: hematite (α-Fe2O3) as a benchmark, *Phys. Chem. Chem. Phys.*, 2011, **13**, 15189.

78 L. Y. Isseroff and E. A. Carter, Importance of reference Hamiltonians containing exact exchange for accurate one-shot GW calculations of Cu2O, *Phys. Rev. B*, 2012, **85**, 235142.